Hydration and restructuring of polar polymer interfaces: Implications in antifouling and responsive materials

Marea J. Blake[1], Seonghan Kim[2], Zhefei Yang[2*], Harry M. Meyer III[1], Scott T. Retterer[2], Jan-Michael Carrillo[2*], Benjamin Doughty[1*]

[1]*Chemical Sciences Division, Oak Ridge National Laboratory, Oak Ridge, TN 37831*

[2]*Center for Nanophase Materials Sciences, Oak Ridge National Laboratory, Oak Ridge, TN 37831*

Hydration and restructuring of polar polymer interfaces: Implications in antifouling and responsive materials

Marea J. Blake[1], Seonghan Kim[2], Zhefei Yang[2*], Harry M. Meyer III[1], Scott T. Retterer[2], Jan-Michael Carrillo[2*], Benjamin Doughty[1*]

[1]*Chemical Sciences Division, Oak Ridge National Laboratory, Oak Ridge, TN 37831*

[2]*Center for Nanophase Materials Sciences, Oak Ridge National Laboratory, Oak Ridge, TN 37831*

Abstract

Manipulating polymer interfaces is crucial for understanding how structure influences function in applications spanning biofouling prevention to energy storage. Moreover, observing how polymers adapt their microscopic structure to changes in their local environment can reveal essential properties that govern their performance in such applications, providing key insights into how to design more effective interfaces. Here, a series of "*grafting-from"* polymer brushes with side chains varying in charge, are probed by sum frequency generation (SFG) and modeled using all-atom molecular dynamics (MD) simulations to elucidate how chemical makeup and charge mediate interfacial restructuring in dry versus hydrated states. Results show that charge, in progressing from nonpolar to cationic to zwitterionic, results in dramatic changes in interfacial structure and overall hydration. While net neutral systems, regardless of bulk phase polarity, show minimal interfacial water structuring, the cationic species exhibits strong bulk water signals from the surface potential. Meanwhile, the polymer brushes themselves restructure in water differently independent of charge, impacting the functional groups that are presented to the aqueous phase. Nonpolar and cationic species for instance undergo a change in alkyl group orientations to accommodate hydrating water molecules, whereas the zwitterionic polymer becomes completely disordered in water. Overall, the structure-based behavior trends presented herein have implications in antifouling applications and responsive material interfaces.

Keywords: polymer coatings, solvation, bio-interface, hydration, soft-matter, nonlinear optics

Introduction

Polymers are often designed to carry out specialized roles based on the chemistry defined by their molecular makeup and immediate chemical environment. From catalyzing reactions to preventing adherence of biomolecules, the macroscopic efficacy of these tasks is controlled by molecular level interactions at the polymer interface. One such interaction hypothesized to play a critical role in antifouling, for instance, is a polymer's response to water. Tuning the hydrophilicity of the polymer composition is key for designing antifouling attributes where the wettability of a polymer surface has a considerable impact on biomolecule adhesion strength and chemical exchange.[1,2] For example, hydrophilic poly(ethylene glycol) (PEG) is often regarded as the canonical antifouling polymer. In PEG brush films fabricated via the "*grafting-from*" strategy, the combination of intrinsic high packing density of polymer brushes and hydrogen bonding between PEG and water molecules make protein and cell attachment thermodynamically unfavorable.[3,4] Similar interfacial

hydration phenomena are seen with polymer surfaces baring positive, negative, or a mixture of charges.[5] Polymers with an overall net charge are not typically employed for antifouling given potential electrostatic interactions with charged biological agents, for example negatively charged bacterial membranes or some marine species.[6–8] Recently, zwitterionic polymer brushes, in which both cationic and anionic constituents reside on the same molecule, have emerged for antifouling applications. In these systems, the formation of strong ion-dipole interactions with water leads to highly structured multi-layer hydration with the added potential to impart better antifouling properties with greater stability.[9–12] Although designed with the promise of increased stability in mind, zwitterionic polymers are typically confined to strict environmental regimes where exposure to extreme conditions, such as that of high ionic strength or high/low pHs, results in unstable and poorly performing coatings.[13–15]

To address stability concerns, zwitterionic polymers containing tertiary amine N-oxides have arisen as a new antifouling material.[16–19] N-oxides are unique in that they consist of an extremely short dipole (i.e., that of a single covalent bond) in comparison to conventional zwitterionic antifouling polymers, such as those containing phosphocholine, sulfobetaine and caboxybetaine moieties.[20–22] As such, they are predicted to exhibit a stronger water affinity while boasting an increased resistance to salts and biomolecule adsorption.[16–19,23,24] Nevertheless, there remains a gap in knowledge about how N-oxide-based polymers adapt in response to changes in their environment. This advance in polymer design, therefore, necessitates systematic studies of the interfacial mechanisms at play when exposed to different environments. Further, understanding adaptability from one environment to another is essential in predicting function for *in situ* antifouling applications. Herein, we use sum frequency generation (SFG) vibrational spectroscopy and all-atom molecular dynamics (MD) to investigate environment-dependent polymer brush restructuring, namely in air versus water, of quartz substrates coated with intermediate precursors towards the synthesis of poly(1-(dimethyl amino)noxide methacrylate) (PNOMA), as shown in Figure 1. Specifically, we probe the constituents that comprise the synthetic route to grow PNOMA from quartz substrates (Figure 1A) from the bromine terminated initiator monolayer (Figure 1B) to poly(2-(dimethylamino)ethyl methacrylate (PDMAEMA) (Figure 1C) to PNOMA (Figure 1D) via a "*grafting-from*" synthetic approach confirmed and characterized by X-ray photoelectron spectroscopy (XPS), Fourier transform infrared spectroscopy (FT-IR), and water contact angles as detailed in the Experimental Methods section below and shown in the Supporting Information.

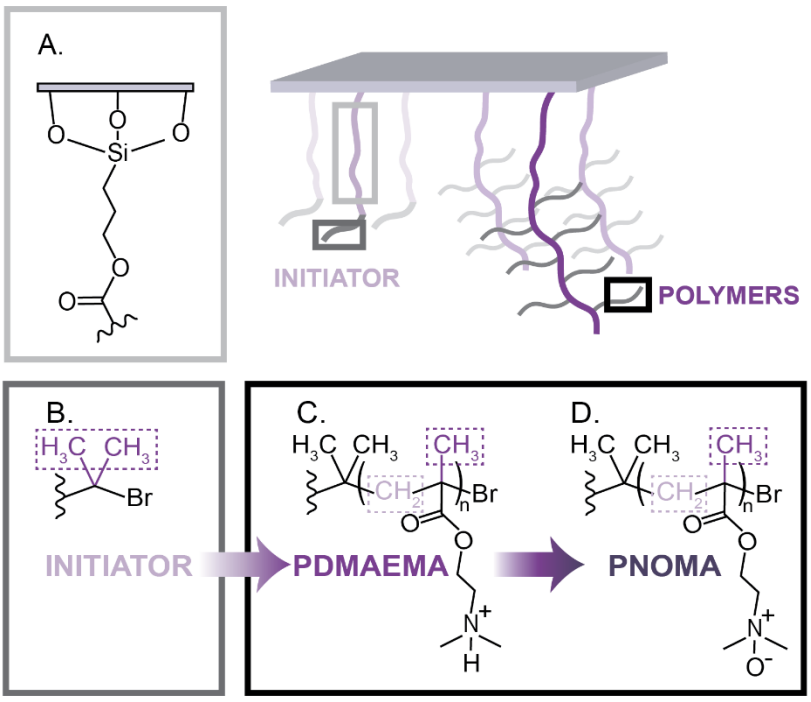

Figure 1. Structures of species under investigation with primary groups contributing to the SFG signals color coded and boxed. Charge states reflect the expected charge at the pH experiments are conducted at. (A) The linker used to grow from quartz for all species. (B) Initiating -Br terminated molecules that lead to the polymerization of (C) PDMAEMA and (D) PNOMA.

SFG is used in this work to provide fundamental insight into how substrate-bound polymers restructure in response to a change in their surroundings. Specifically, by probing both the -CH and -OH spectral regions, we can map restructuring of polymer moieties, (i.e., the functional groups highlighted in Figure 1) while reporting on the organization of interfacial water. Further, in conjunction with all-atom MD simulations, the average orientational tilt angle of the functional groups relative to the substrate surface are extracted to quantify the restructuring from one solvent phase to another and provide a rich view of the interfacial chemistry and solvation that could lead to the novel anti-fouling properties. Though SFG has been previously employed to study N-oxide structures, in this work we emphasize the insight gained in going from a state of no hydration in air to fully saturating the polymer surface with water to understand the role of the charge that the polymers bare in the context of hydration and antifouling.[25] Additionally, all-atom MD simulations reveal how the hydration and charge pairings along the polymer backbone differ between systems in creating free space near the surface, which is important in understanding the molecular-level interactions underpinning zwitterionic polymer hydration and antifouling behaviors. The information gathered from these results is useful in predicting the effectiveness of polymers at warding off fouling species while providing new chemical insight into the role of hydration in defining key interfacial interactions that can be tuned in next generation materials.

Results and Discussion

In order to determine how the polymer brushes restructure in response to the environment they reside in, SFG was used to monitor the functional groups on the polymer in air and then in water, as described below in the Experimental Methods. SFG is inherently sensitive to the orientations of molecule populations confined to a surface, and therefore an ideal probe of interfacial ordering.[26–29] While a well-ordered film with like-constituents is expected to provide significant SFG signals, the plane in which the molecules are aligned has a considerable impact on the observed spectra. For instance, SFG predominantly probes transitions directed *out* of the interfacial plane. Symmetry *in* the interfacial plane from a well ordered monolayer, however, can give rise to a weak SFG response due to azimuthal averaging that might be otherwise attributed to a poorly ordered interface.[27,30] By probing various SFG polarization combinations, however, a distinction between ordering and orientation can be unraveled, as discussed below. Here, spectra were measured (details given in the Materials and Methods section) in both SSP and PPP polarization combinations to probe symmetric and asymmetric stretches, respectively, in the -CH stretching region (<3000 cm^{-1}).

The SSP spectra measured in air are shown in Figure 2A where four dominant signatures are present. Peaks at (a) ~2845 cm^{-1} and (b) ~2865 cm^{-1} are assigned to the $-CH_2$ and $-CH_3$ symmetric stretches and peaks at (c) ~2925 cm^{-1} and (d) ~2940 cm^{-1} are assigned to $-CH_2$ and $-CH_3$ Fermi resonances (FRs) with contributions from unresolved asymmetric stretches for all three samples.[27,31] The origin of these vibrational resonances differs, however, depending on the sample (e.g., initiator vs. polymer (PDMAEMA and PNOMA)). Since the initiator sample lacks repeat units, the $-CH_2$ SFG signals arise from the linker that attaches the polymer to the quartz substrate (Figure 1A) while the $-CH_3$ signals are from the methyl groups adjacent to the terminal bromine, as illustrated in Figure 1B. For PDMAEMA and PNOMA, however, the $-CH_2$ and $-CH_3$ peaks most likely originate from the methacrylate backbone of the repeat monomer units with $-CH_2$ contributions from the pendant groups (highlighted in Figure 1). Although the SFG response from the linker is not isolated from that of the polymers, given the number densities of $-CH_2$ and $-CH_3$ groups from the grafted polymers and the respective changes based on chemistry and solvation, the observed signals are taken to largely arise from the polymers. It should be noted that signals near ~2930 cm^{-1} could also arise from the methyl groups residing on the N-oxide moiety for PNOMA, although they are not resolved from the FRs.[32,33] Similarly, a small shoulder is seen at ~2750 cm^{-1} for PDMAEMA that could originate from the $N-CH_3$ groups.[34,35] In the PPP spectra, asymmetric $-CH_2$ and $-CH_3$ stretches are observed at (e) ~2910 cm^{-1} and (f) ~2950 cm^{-1}, respectively, with minimal contributions from symmetric stretches defined above, as seen in Figure 1B.[27,31]

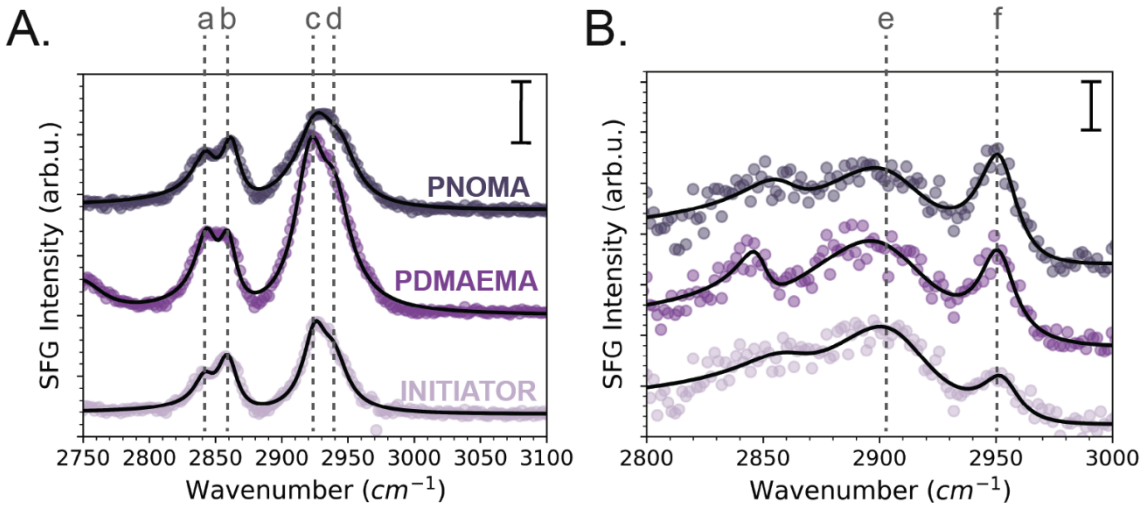

Figure 2. (A) SSP and (B) PPP SFG spectra of the polymer/air interface. Plots are offset for clarity. Colored spectra correspond to the data for structures shown in Figure 1, also defined in (A), while the overlayed solid black lines are the fits to the data. Scale bars for (A) and (B) are equal to 1 and 0.2 arbitrary units, respectively. Dashed lines with lower case letter labels correspond to peak positions assigned in the text.

When the coatings are introduced to water, the SSP spectra in the -CH region drastically changes. In air, both methylene and methyl resonances are observed for all three samples, however, when exposed to water, only one or the other dominates the spectra, as shown in Figure 3A. For instance, in water, the initiator control sample displays prominent peaks at ~2860 cm^{-1} and ~2940 cm^{-1}, indicating that the -CH_3 moieties are more ordered than the -CH_2 groups which have most likely restructured either in an isotropic fashion and/or lie parallel to the interface owing to the greatly reduced -CH_2 signals expected at ~2845 cm^{-1}. A similar result is found for PDMAEMA where the methyl groups along the polymer backbone remain aligned out of the interfacial plane as compared to the -CH_2 groups, as evidenced by negligible -CH_2 signals. PNOMA, however, tells a different story when placed in water where differences in the SFG response from the initiator and PDMAEMA films are observed. For PNOMA, broad unresolvable resonances are seen at ~2850 cm^{-1} and ~2930 cm^{-1} in the SSP spectrum (Fig. 3A) while no peaks are identifiable in the PPP spectrum (data not shown). These observations indicate that the PNOMA polymer backbone becomes more disordered when placed in an aqueous environment with the pendant groups for taking on surprisingly isotropic distributions.

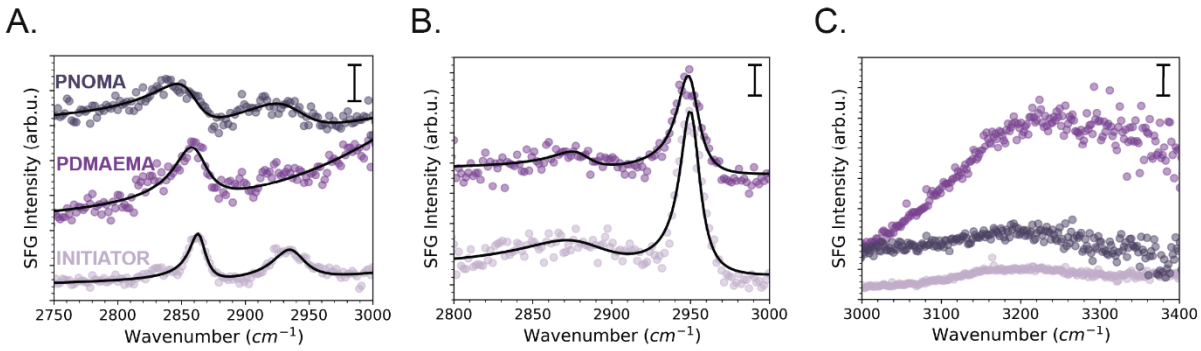

Figure 3. SFG spectra of the polymer/water interface for the initiator (lavender, bottom), PDMAEMA (plum, middle) and PNOMA (eggplant purple, top). Plots in A and B are offset for clarity. (A) SSP and (B) PPP spectra in the CH region. (C) SSP spectra in the OH region that are not offset from one another. Colored spectra correspond to the structures defined in Figure 1 while the black lines overlayed are the fits to the data. Scale bars for (A), (B) and (C) are equal to 0.5, 0.2 and 1 arbitrary units, respectively.

To further disentangle orientational and ordering effects on the SFG response, average tilt angles for specific functional groups can be estimated from SFG experiments by comparing the intensities of the symmetric and asymmetric methyl stretches observed from SSP and PPP spectra, respectively, in Figures 2 and 3.[27] To extract the mode specific amplitudes needed for orientational analysis, SFG data were fit to

(Eq.1)

$$I_{SFG} \propto \left| \sum_{q} \frac{A_q}{\omega_{IR} - \omega_q + i\Gamma_q} + \chi_{NR}^{(2)} e^{i\Phi} \right|^2$$

where I_{SFG} is the observed SFG intensity, which is taken to be a coherent sum of Lorentzians with amplitude, linewidth, and frequency expressed as A_q, Γ_q, and ω_q, respectively, for the q^{th} vibrational mode. The non-resonant and phase contributions are given by $\chi_{NR}^{(2)}$ and ϕ,[36,37] which is important for studies of aqueous interfaces where contributions from bulk field aligned water appear. We note here that visual comparisons of SFG intensity spectra are limited by the interference between resonances, the non-resonant background, and contributions from polarized bulk water via the surface potential. To obtain molecular insight into these surfaces the SFG spectra are fit to Eq. 1. Peak intensities obtained from fitting report on both the number density and the average orientation of a given functional group.[27,30] In addition to these effects, however, FR bands are extremely sensitive to local intermolecular polymer-polymer interactions[38,39], impacting the FR peak positions and intensities. These responses interfere with the out of phase asymmetric -CH_3 vibrations[30] giving rise to different apparent peak intensities in the measured intensity spectra. A summary of peak positions and amplitudes is given in the Supporting Information along with the physical constants used in orientational analyses. The fitting results show the FR bands vary

depending on the material and solvation environment, as expected given different chain-chain interactions. Further, a weak -CH_2 peak might be observed in the data plotted in Figure 3a; however, attempts to reliably fit these peaks resulted in large parameter uncertainties (~ 50%) with no reasonable improvement in the quality of fit. As such, the minimal model used in fitting here is useful to understand *trends* in the average orientation and should not be taken as absolute. Additionally, to account for the broad OH stretching signals observed >2950 cm^{-1}, we included a single broad OH resonance in the fitting of the initiator and PDMAEMA samples, which interfere with the CH stretches. The OH contribution to in the PNOMA sample is more subtle and evident by different by $\chi_{NR}^{(2)}$ and ϕ terms describing the same interference effect.

It was found that the -CH_3 groups for the initiator undergo the largest restructuring from an average orientational tilt angle of 17 ± 4° with respect to the surface normal in air to 27 ± 2° in water, as shown in Figure S1. This change in tilt angle for initiator films suggests the -CH_3 groups are pushed towards the quartz surface due to the hydrophobic nature of the initiator terminal groups. Although following the same qualitative trend, the change in orientation for PDMAEMA is not as dramatic as the initiator sample, showing only a change of ~4° with a tilt angle of 26 ± 3° in water. Here we note that the increase in tilt angle of the backbone CH_3 groups on submersion into water are in line with an extended backbone structure, where the pendant arms would be directed more parallel to the surface plane, though the direction of which (*e.g.*, up vs. down), is ambiguous from the homodyne SFG methods used in this work.[40,41] As mentioned above, asymmetric methyl stretches for PNOMA are not seen once the polymer is placed in water, therefore prohibiting orientational analysis. However, since the PPP response from these vibrations should increase with tilt angle, the weak SSP and negligible PPP signals from PNOMA indicate that SFG is reporting on increase disorder and not on azimuthal averaging.[27]

To better understand the orientation difference between PDMAEMA and PNOMA, all-atom MD simulations were conducted, further detailed in the Experimental Methods section. Figures 4A and 4B show the orientational angle analysis of each component in PDMAEMA and PNOMA. The ordering parameter, P_2, was calculated using the second order Legendre polynomial,

Eq. (2)

$$P_2(\cos\theta) = \frac{1}{2}(3\cos^2\theta - 1)$$

where θ is the angle between the vectors along the Z-axis, defined as the normal to the quartz surface, and each component (i.e., -CH_2, -CH_3 and -NO/-NH groups), as illustrated in Figure S2. P_2 values close to -0.5 and 1.0 represent perpendicular and parallel orientations relative to the Z-axis, respectively, while values around 0 indicate isotropic media. For instance, within the brush region (20 Å < Z < 40 Å), the P_2 values for PNOMA's moieties—CH_2 (blue, -0.115 ± 0.011), CH_3 (yellow, -0.277 ± 0.005), NO (red, -0.228 ± 0.006)—are closer to zero than those for PDMAEMA—CH_2 (blue, -0.175 ± 0.011), CH_3 (yellow, -0.392 ± 0.005), NH (black, -0.277 ± 0.005). This indicates that PNOMA is more disordered in water than PDMAEMA, a trend that is supported by the SFG experimental data. As previously reported,[42] cationic PDMAEMA exhibits repulsive interactions between chains, resulting in vertically aligned polymer chains extending into

the bulk. To quantify interchain spacing, the radial distribution function, g(r), is calculated between the N atoms in the pendant groups in PNOMA and PDMAEMA (Fig. 4C). The results show that PDMAEMA exhibits a sharp peak around 8 Å, whereas PNOMA displays a shoulder and a broader peak at approximately 5 Å and 8 Å, respectively. The presence of a single peak at a longer distance in PDMAEMA reflects interchain repulsion, which leads to greater internal spacing and minimizes interchain interactions (Figure S3A). In contrast, the appearance of broader N-N distributions in PNOMA, including one at a shorter distance, suggests that zwitterionic PNOMA adopts a more collapsed structure due to attractive interchain interactions, resulting in reduced spacing between chains and consequently more random orientations (Figure S3B). These trends are in line with SFG measurements above, providing a correspondence between experiment and simulation.

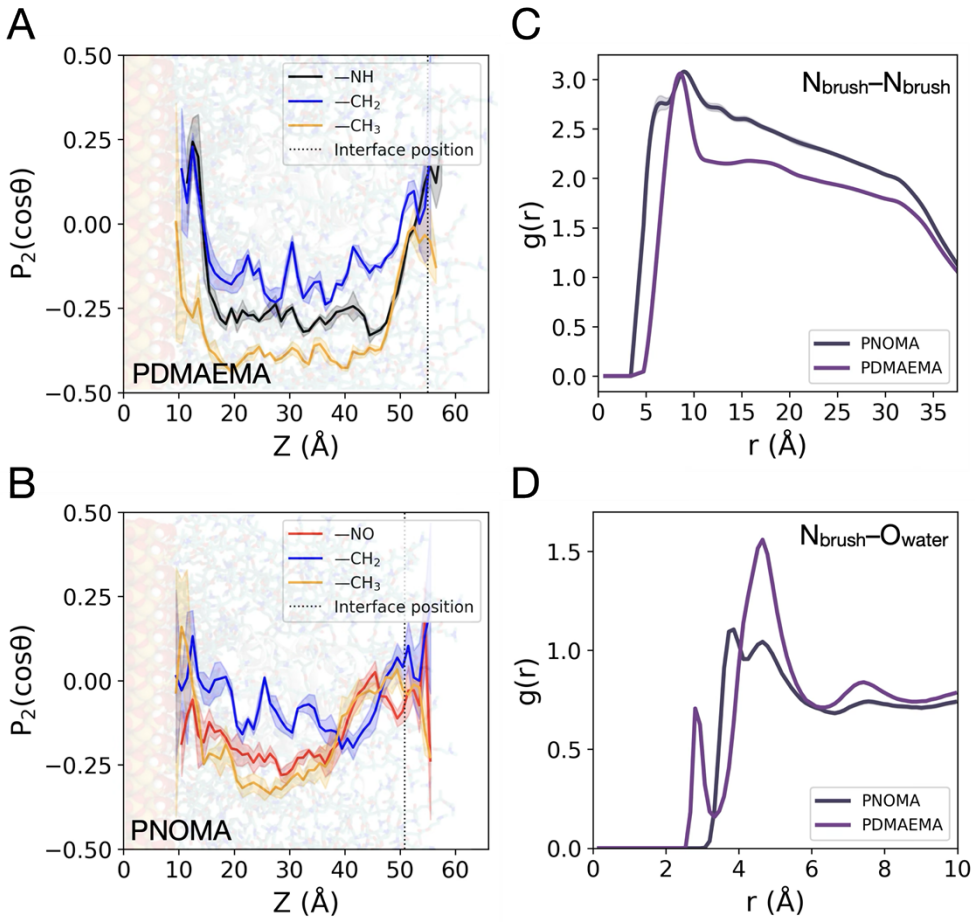

Figure 4. (A–B) Orientational angle analysis of (A) PDMAEMA and (B) PNOMA. The angle was calculated between vectors along the *Z*-axis and each moiety, i.e., –NH (black), –NO (red), $–CH_2$ (blue), and $–CH_3$ (yellow) groups, highlighted in Figure 1C,D. The interface position was taken from our prior study.[42] (C) Radial distribution functions, g(r), between the N atoms in pendant groups in PNOMA and PDMAEMA. (D) g(r) between the N atoms in pendant groups and the O atoms of water molecules in PNOMA and PDMAEMA.

This interplay between polymer structure and water can be investigated by considering OH stretches at frequencies >3000 cm^{-1} in SFG experiments. From the spectra shown in Figure 3C, it is apparent that PDMAEMA most strongly organizes water molecules along the polymer/water interface due primarily to the net positive surface potential at pH 6-7, which was employed in this work (pKa of PDMAEMA ~7.5[43]). Larger OH signals near ~3200 cm^{-1} indicate stronger hydrogen bonding and effects of charge in polarizing bulk water – though separating these effects is not the purpose of this work.[44] The initiator and PNOMA samples, meanwhile, show minimal bulk water organization due to the net zero charge densities on the molecule/polymer, with contributions from unreacted O^- species on the quartz interface presumed to provide some bulk water ordering most prominently found in the initiator sample. The lack of notable strong hydrogen bonding signals at the PNOMA interface is expected due to the close proximity of the charged atoms and the opposite orientation the water molecules would take around the collapsed structures found in simulations, further discussed below. This observation is in line with reports of strongly bound water at other N-oxide polymer interfaces and the role of this characteristic in its potential for antifouling abilities.[16,25,45–47]

To corroborate measurements in understanding how water molecules interact with the pendant groups in PDMAEMA and PNOMA brushes, g(r) is calculated between the nitrogen atoms of the pendant groups and the oxygen atoms of water molecules. Note that the g(r) values fall slightly below 1 at larger distances due to reduced local water density, which results from the presence of the substrate. As shown in Figure 4D, PDMAEMA shows a sharper and higher g(r) peak at a shorter distance compared to PNOMA, indicating a strongly bound hydration shell with higher water density near the pendant groups. This is attributed to the greater internal spacing within the brush environment (Fig. 4C) and the positively charged amine groups in PDMAEMA (Fig. 1C), which promote stronger electrostatic interactions with water. In contrast, PNOMA shows a smaller spacing (~1 Å; 4.9 Å – 3.9 Å) between the first and second peaks of g(r), compared to PDMAEMA (~ 1.9 Å; 4.9 Å – 3 Å), suggesting that water interactions with nitrogen atoms are influenced by nearby oxygen atoms in PNOMA. The average number of hydrogen bonds between water and the polymer brushes over the last 30 ns of simulations is plotted in Figure S4, which further highlights the stronger water–polymer interactions in PNOMA compared to PDMAEMA. This observation supports what is seen in SFG experiments where weak -OH signals are most likely due to an introduction of symmetry of water molecules surrounding the N-oxide structure. While g(r) does not directly reflect hydrogen bonding strength, it effectively captures differences in water accessibility and local density around the pendant groups. As a result, the pendant groups in PDMAEMA are better able to maintain structural order, as shown in Figure 3C.

Conclusions

Here, the combination of SFG and all-atom MD simulations are used to understand how the charge of polymer brushes grafted to quartz substrates at similar grafting densities affects 1) molecule-level orientation in two different dielectric environments and 2) the ordering of water at the interface of these coatings to provide insight into how these coating characteristics may behave in anti-fouling applications. For the polymer brushes, we show that positively charged PDMAEMA

similarly retains order on exposure to water, whereas zwitterionic PNOMA coatings adopt a condensed isotropic distribution, schematically illustrated in Figure 5. This observation is attributed to possible interchain interactions due to the zwitterionic nature of PNOMA, which was manifested in simulations as collapsed structures and supported by SFG measurements as small responses. PDMAEMA, however, significantly orders water molecules due to the positively charged amine groups in the pendant groups (Figure 5) such that chains extend into the bulk water phase to minimize charge repulsion between pendant arms. Overall, the results presented herein can potentially inform on the design of polymer interfaces for minimizing biomolecule interactions in environments with fluctuating levels of hydration.

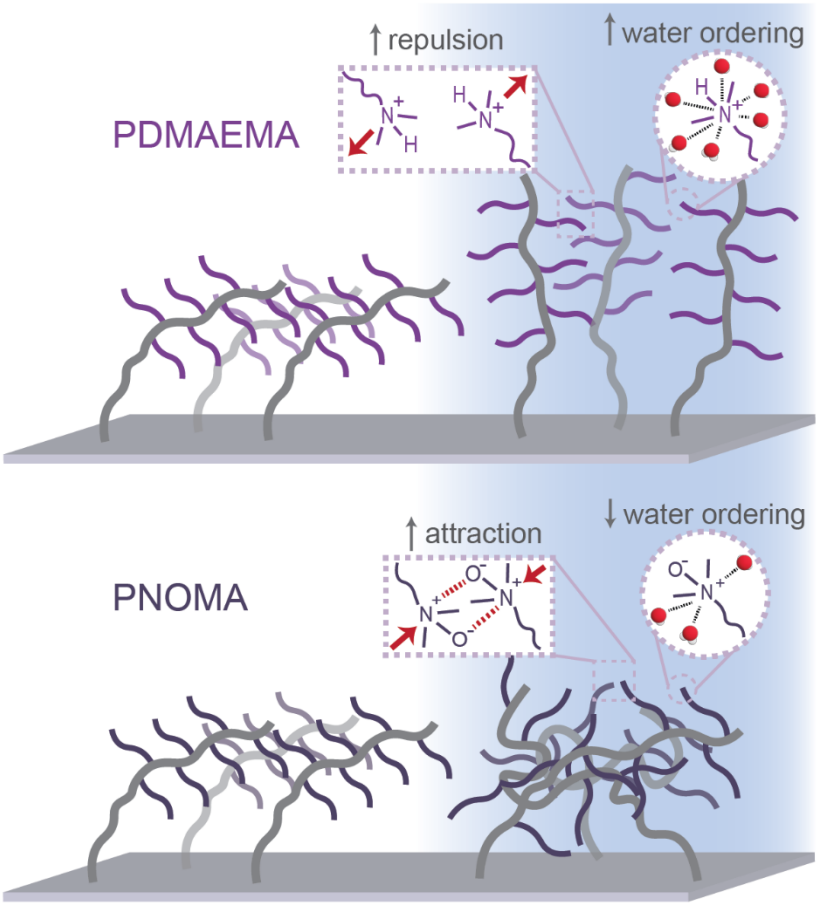

Figure 5. Cartoon schematic illustrating polymer restructuring going from (left) air to (right) water of (top) cationic PDMAEMA and (bottom) zwitterionic PNOMA with propensity for interchain interactions and water ordering characteristics highlighted in water.

Experimental Methods

Polymer Preparation and Characterization

Cleaned and hydroxylated via 1 hour UV/Ozone treatment quartz substrates (2.5 cm × 2.5 cm × 0.2 mm) were coated with the ATRP initiator (3-(trimethoxysilyl)propyl 2-bromo-2-methylpropanoate) following literature preparations.[48] Briefly, to attach the ATRP initiator (Figures 1A & 1B), the substrates were incubated with the initiator in a toluene solution at 90°C for 12 hours. To graft PDMAEMA (Figure 1C) onto the surface, the initiator-coated quartz substrates were placed in a degassed isopropanol solution containing the monomer (2-(dimethylamino)ethyl methacrylate, DMAEMA, 3M), CuBr (12 mM), N,N′,N″,N″-pentamethyldiethylenetriamine (PMDETA, 24 mM) and ethyl α-bromoisobutyrate (6 mM) for 24 hours at 40°C C to obtain PDMAEMA polymers with a targeted degree of polymerization of 500. The PNOMA-coated (Figure 1D) substrate was prepared by oxidizing the PDMAEMA-coated substrate with meta-chloroperoxybenzoic acid (0.1 M in methanol). This synthesis route guarantees consistent grafting densities across the three species[49] and therefore allows one-to-one comparison of the orientation and restriction of functional groups with varying charge states from nonpolar (initiator) to charged (PDMAEMA) to zwitterionic (PNOMA).

Surface grafting of initiators and polymers was confirmed X-ray photoelectron spectroscopy (XPS) and Fourier transform infrared spectroscopy (FT-IR), respectively.

XPS was performed using a Thermo Scientific (Waltham, MA, USA) Model Nexsa G2 XPS instrument. The instrument utilizes monochromated, micro-focused, Al Kα X-rays (1486.6 eV) with a variable spot size (i.e., 30-400 μm). Analyses of the sample was performed with the 400 μm X-ray spot size for maximum signal and to obtain an average surface composition over the largest possible area. The instrument has a hemispherical electron energy analyzer equipped with a 128-channel detector system. Base pressure in the analysis chamber is typically 2×10^{-9} mbar or lower. The quartz samples were prepared for analysis by attaching them directly to the XPS sample holder using metal clips. Due to the X-ray labile nature of bromine[50], the following experimental sequence was used to minimize X-ray exposure. The initial analysis was done by acquiring a set of "snapshot" spectra for Br_{3d}, C_{1s}, O_{1s}, and Si_{2p} and then repeated a total of 30 times. Snapshot spectra were acquired using the full 128 channel electron detector to obtain the full core level spectrum in several seconds. Each iteration of collecting the four snapshot spectra was ~40 seconds for a total X-ray exposure time of ~20 min. After the initial acquisition of Br, C, O and Si, a wide energy range survey spectrum was acquired. All spectra were acquired with the charge neutralization flood gun turned on to maintain a stable analysis condition. The flood gun uses a combination of low energy electrons and argon ions for optimum charge compensation. The typical pressure in the analysis chamber with the flood gun operating is 2×10^{-7} mbar. Data were collected using the Thermo Scientific Avantage XPS software package (v.6.8.1) and analyzed using CasaXPS. As shown in Figure S4a, the peak at 70.2 eV in the Br_{3d} spectrum indicated the presence of the Br-containing ATRP initiator. In the C_{1s} spectrum (Figure S4b), peak deconvolution revealed distinct carbon atoms at 284.4 eV (C-C), 285.8 eV (C-O) and 288.5 eV (C=O), further verifying the initiator on surface. In the survey spectrum (Figure S4c) acquired after the snapshot spectra, only the C_{1s} peak was detected to confirm the initiator presence, while the Br_{3d} signal was not detected due to bromine's labile nature under X-ray exposure.

The polymer coatings were characterized by FT-IR using a Bruker Vertex 70 FT-IR spectrometer, equipped with a VariGATR™ grazing angle attenuated total reflection (ATR) accessory (Harrick Scientific Products Inc.), and a $N_{2(l)}$-cooled mercury-cadmium-telluride (LN-MCT Narrow) detector. IR spectra were recorded in a wavelength range from 650 to 4000 cm^{-1}, with a scan number of 128, a resolution of 4 cm^{-1} and an incident angle of 65°. Sample spectra were collected by pressing the polymer-coated surface on the ATR crystal, and a background spectrum was collected without substrate. As shown in Figure S5, the ester carbonyl absorption at 1728 cm^{-1} representing the methacrylate backbone verified the presence of both PDMAEMA and PNOMA on the substrate. After oxidation of PDMAEMA on the surface, signals at 2822 cm^{-1} and 2770 cm^{-1} representing symmetric and asymmetric C-H stretching for $-N(CH_3)_2$ respectively were absent, indicating successful conversion from PDMAEMA to PNOMA, consistent with the literature.[24]

The thicknesses of PDMAEMA and PNOMA brushes on the substrates were determined by X-ray reflectometry (XRR), which was performed on a Rigaku SmartLab X-ray diffractometer equipped with a PhotonMax high-flux 9 kW rotating anode and Cu Kα radiation having a wavelength of 1.54 Å. The sample was aligned and measured on a motorized adjustable R_x–R_y sample stage capable of properly positioning the sample along the *x*–*y* direction. Both the incidence and detector slit had a width of 0.075 mm. The reflectivity measurement was performed at incidence angles of 0–6.0000° using a 0.0040° increment and a rate of 0.4000° per min. The film thickness, density, and roughness profiles were constructed using Rigaku SmartLab Studio II. The thickness for PDMAEMA and PNOMA brushes were 24.9 ± 0.7 and 25.7 ± 0.8 nm, respectively.

Water contact angles were measured to characterize the wettability of surface coatings using a Krüss DSA30 drop shape analyzer. With a 2.5-μL water droplet released onto the surface, multiple measurements were performed at 1 frame per second for 1 min to obtain average results. Measurements on three different spots were collected for each sample to obtain the average value and standard deviation. As shown in Table S5, the water contact angles were ~70°, 53° and 39° for the initiator-, PDMAEMA- and PNOMA-coated surfaces, respectively. The lower contact angle for PNOMA samples was attributed to its hydrophilic zwitterionic structure.

Sum Frequency Generation (SFG) Measurements

A homebuilt instrument, described in detail previously, was used to perform the SFG measurements.[51] Briefly, collinear narrowband near-infrared (NIR)[52,53] and broadband IR were incident on the top surface of the quartz substrates at ~60° relative to the surface normal to reach the buried polymer/air or polymer/water interface, as illustrated in Figure S7. The polymer layers are sufficiently thin, however, that SFG signals originating from both the quartz/polymer and polymer/solvent interfaces are indistinguishable from one another.[54–56] The quartz substrates were suspended over a piranha-cleaned Teflon dish with an empty reservoir underneath for polymer/air measurements. For the polymer/water measurements, the reservoir was filled with ultrapure water (18.2 MΩ·cm, pH ~ 6). SFG signals generated from the interface of interest were then collimated and filtered before polarization selection. Transmitted light was dispersed and detected with a spectrometer and CCD camera.

All measurements were performed under different polarization combinations; for instance, the SSP polarization where the SFG and NIR sources were S-polarized, and the IR source was P-polarized, report predominantly on symmetric stretches more parallel to the surface normal. Measuring asymmetric stretches in the PPP combination can permit estimates of functional group orientation tilt angles. Spectra were collected for 300 seconds. For SSP measurements, data were collected with the IR centered at 2700 cm^{-1}, 2900 cm^{-1}, 3100 cm^{-1} and 3300 cm^{-1}. The resulting spectra were background subtracted, stitched together and finally divided by similarly stitched gold reference spectra taken at the same center IR frequencies.[57,58] Before stitching, each data and gold spectra were truncated at 25% of the maximum intensity of the gold spectra to limit contributions from noise to the final stitched spectra.[57] For PPP measurements, the IR was centered at 2900 cm^{-1}. Resulting data were background subtracted and divided by the corresponding gold reference spectrum.

All-Atom Molecular Dynamics (MD) Simulations

All-atom MD simulations were performed using NAMD.[59] Force fields employed include CGenFF[60–62] for the polymer, IFF[63] for the silica surface, with the TIP3P water model.[64] van der Waals interactions were treated using a force-based switching function that smoothly decayed between 10 and 12 Å. Long-range electrostatics were calculated via the particle-mesh Ewald (PME) method,[65] employing a grid spacing of 1 Å and a sixth-order B-spline interpolation. Hydrogen-involving bond lengths were constrained using the SHAKE algorithm.[66]

The modeling procedures for constructing PDMAEMA and PNOMA brushes used in this study were based on our previous study.[42] CHARMM-GUI Nanomaterial Modeler[67] was employed to build the α-quartz, with surface oxygen atoms modified into silanol groups to mimic conditions at pH 7. A grafting density of 0.4 chains/nm^2 was used and polymer chains with a degree of polymerization of 20 were randomly placed on the quartz surface, after which covalent bonds were formed between the surface and each linker, and between each linker and its corresponding polymer chain. To equilibrate systems, 200 ns of MD simulations were performed, and the last 30 ns trajectories were used for analysis. Equilibration was carried out in the NVT ensemble with positional and dihedral restraints, which were gradually reduced. Subsequent production simulations were run under the NPT ensemble with periodic boundary conditions at 303.15 K and 1.01325 bar, using Langevin dynamics (damping coefficient of 1 ps^{-1}) for temperature control and the Langevin piston method for pressure control.[68] Three independent simulations were conducted for each system for statistical results.

Author Contributions

M.J.B. and S.K. are equally contributed to this study.

M.J.B.: Conceptualization, experiments, analysis, visualization, and writing—original draft, review, and editing; S.K.: conceptualization, MD simulation, analysis, visualization, and writing—original draft, review, and editing; Z.Y.: conceptualization, experiments, writing—original draft, review, and editing; H.M.M. III: XPS measurements and analysis; S.T.R. and J.-M.C.: supervision and writing—review and editing; B.D.; conceptualization, analysis, supervision and writing—review and editing.

Corresponding Authors

* Zhefei Yang – yangz@ornl.gov

* Jan-Michael Y. Carrillo – carrillojy@ornl.gov

* Benjamin Doughty – doughtybl@ornl.gov

Acknowledgements

Authors were supported by the Department of Energy, Office of Science FWP ERKCZ64, Structure Guided Design of Materials to Optimize the Abiotic-Biotic Material Interface, as part of the Biopreparedness Research Virtual Environment Initiative.

Work by S.K., Z.Y., S.T.R, and J-M.C was performed at the Center for Nanophase Materials Sciences, the U.S. Department of Energy Office of Science User Facility operated at Oak Ridge National Laboratory. This research used resources of the Oak Ridge Leadership Computing Facility (OLCF) at Oak Ridge National Laboratory, which is supported by the Office of Science of the U.S. Department of Energy under Contract No. DE-AC05-00OR22725.

Supporting Information

Fitting results for SFG data (Tables S1 & S2), Details of SFG orientational analysis and plotted results (Figure S1), Table of SFG orientational analysis results and parameters (Tables S3 & S4), definitions of angles used for MD orientational analysis (Figure S2), MD snapshots of polymer brush configurations (Figure S3), MD simulation of number of hydrogen bonds between water and polymer brushes (Figure S4), XPS spectra of Initiatory coatings (Figure S5), FTIR spectra of polymer coatings (Figure S6), Water contact angle data for polymer samples (Table S5), schematic of sample preparation geometry for SFG experiments (Figure S7).

References

(1) Liu, Y.; Liu, Y.; Wu, Y.; Zhou, F. Tuning Surface Functions by Hydrophilic/Hydrophobic Polymer Brushes. *ACS Nano* **2025**, *19* (12), 11576–11603. https://doi.org/10.1021/acsnano.4c18335.

(2) Chen, S.; Li, L.; Zhao, C.; Zheng, J. Surface Hydration: Principles and Applications toward Low-Fouling/Nonfouling Biomaterials. *Polymer* **2010**, *51* (23), 5283–5293. https://doi.org/10.1016/j.polymer.2010.08.022.

(3) Lowe, S.; O'Brien-Simpson, N. M.; Connal, L. A. Antibiofouling Polymer Interfaces: Poly(Ethylene Glycol) and Other Promising Candidates. *Polym. Chem.* **2014**, *6* (2), 198–212. https://doi.org/10.1039/C4PY01356E.

(4) Zhang, K.; Huang, H.; Hung, H.-C.; Leng, C.; Wei, S.; Crisci, R.; Jiang, S.; Chen, Z. Strong Hydration at the Poly(Ethylene Glycol) Brush/Albumin Solution Interface. *Langmuir* **2020**, *36* (8), 2030–2036. https://doi.org/10.1021/acs.langmuir.9b03680.

(5) Leng, C.; Huang, H.; Zhang, K.; Hung, H.-C.; Xu, Y.; Li, Y.; Jiang, S.; Chen, Z. Effect of Surface Hydration on Antifouling Properties of Mixed Charged Polymers. *Langmuir* **2018**, *34* (22), 6538–6545. https://doi.org/10.1021/acs.langmuir.8b00768.

(6) Do, J.; Kang, S. M. Effect of Surface Charges in Polymer Coatings on Antifouling Performance in Marine Environments with Sediment. *Langmuir* **2024**, *40* (37), 19644–19653. https://doi.org/10.1021/acs.langmuir.4c02304.

(7) Guo, S.; Jańczewski, D.; Zhu, X.; Quintana, R.; He, T.; Neoh, K. G. Surface Charge Control for Zwitterionic Polymer Brushes: Tailoring Surface Properties to Antifouling Applications. *Journal of Colloid and Interface Science* **2015**, *452*, 43–53. https://doi.org/10.1016/j.jcis.2015.04.013.

(8) Yang, W.; Lin, P.; Cheng, D.; Zhang, L.; Wu, Y.; Liu, Y.; Pei, X.; Zhou, F. Contribution of Charges in Polyvinyl Alcohol Networks to Marine Antifouling. *ACS Appl. Mater. Interfaces* **2017**, *9* (21), 18295–18304. https://doi.org/10.1021/acsami.7b04079.

(9) Chen, Z. Surface Hydration and Antifouling Activity of Zwitterionic Polymers. *Langmuir* **2022**, *38* (15), 4483–4489. https://doi.org/10.1021/acs.langmuir.2c00512.

(10) Ladd, J.; Zhang, Z.; Chen, S.; Hower, J. C.; Jiang, S. Zwitterionic Polymers Exhibiting High Resistance to Nonspecific Protein Adsorption from Human Serum and Plasma. *Biomacromolecules* **2008**, *9* (5), 1357–1361. https://doi.org/10.1021/bm701301s.

(11) Schlenoff, J. B. Zwitteration: Coating Surfaces with Zwitterionic Functionality to Reduce Nonspecific Adsorption. *Langmuir* **2014**, *30* (32), 9625–9636. https://doi.org/10.1021/la500057j.

(12) Jiang, S.; Cao, Z. Ultralow-Fouling, Functionalizable, and Hydrolyzable Zwitterionic Materials and Their Derivatives for Biological Applications. *Advanced Materials* **2010**, *22* (9), 920–932. https://doi.org/10.1002/adma.200901407.

(13) Du, Y.; Gao, J.; Chen, T.; Zhang, C.; Ji, J.; Xu, Z.-K. Understanding the Oxidative Stability of Antifouling Polymer Brushes. *Langmuir* **2017**, *33* (29), 7298–7304. https://doi.org/10.1021/acs.langmuir.7b01681.

(14) Zhang, Z.; Moxey, M.; Alswieleh, A.; Morse, A. J.; Lewis, A. L.; Geoghegan, M.; Leggett, G. J. Effect of Salt on Phosphorylcholine-Based Zwitterionic Polymer Brushes. *Langmuir* **2016**, *32* (20), 5048–5057. https://doi.org/10.1021/acs.langmuir.6b00763.

(15) Alswieleh, A. M.; Cheng, N.; Canton, I.; Ustbas, B.; Xue, X.; Ladmiral, V.; Xia, S.; Ducker, R. E.; El Zubir, O.; Cartron, M. L.; Hunter, C. N.; Leggett, G. J.; Armes, S. P. Zwitterionic Poly(Amino Acid Methacrylate) Brushes. *J. Am. Chem. Soc.* **2014**, *136* (26), 9404–9413. https://doi.org/10.1021/ja503400r.

(16) Li, B.; Jain, P.; Ma, J.; Smith, J. K.; Yuan, Z.; Hung, H.-C.; He, Y.; Lin, X.; Wu, K.; Pfaendtner, J.; Jiang, S. Trimethylamine N-Oxide–Derived Zwitterionic Polymers: A New

Class of Ultralow Fouling Bioinspired Materials. *Science Advances* **2019**, *5* (6), eaaw9562. https://doi.org/10.1126/sciadv.aaw9562.
(17) Feng, Z.; Feng, X.; Lu, X. Bioinspired N-Oxide-Based Zwitterionic Polymer Brushes for Robust Fouling-Resistant Surfaces. *Environ. Sci. Technol.* **2023**, *57* (18), 7298–7308. https://doi.org/10.1021/acs.est.3c00128.
(18) Burmeister, N.; Zorn, E.; Farooq, A.; Preuss, L.; Vollstedt, C.; Friedrich, T.; Mantel, T.; Scharnagl, N.; Rohnke, M.; Ernst, M.; Wicha, S. G.; Streit, W. R.; Maison, W. Surface Grafted N-Oxides Have Low-Fouling and Antibacterial Properties. *Advanced Materials Interfaces* **2023**, *10* (35), 2300505. https://doi.org/10.1002/admi.202300505.
(19) Luc, V.-S.; Lin, C.-C.; Wang, S.-Y.; Lin, H.-P.; Li, B.-R.; Chou, Y.-N.; Chang, C.-C. Antifouling Properties of Amine-Oxide-Containing Zwitterionic Polymers. *Biomacromolecules* **2023**, *24* (11), 5467–5477. https://doi.org/10.1021/acs.biomac.3c00948.
(20) Zhang, Z.; Chao, T.; Chen, S.; Jiang, S. Superlow Fouling Sulfobetaine and Carboxybetaine Polymers on Glass Slides. *Langmuir* **2006**, *22* (24), 10072–10077. https://doi.org/10.1021/la062175d.
(21) Cao, B.; Tang ,Qiong; and Cheng, G. Recent Advances of Zwitterionic Carboxybetaine Materials and Their Derivatives. *Journal of Biomaterials Science, Polymer Edition* **2014**, *25* (14–15), 1502–1513. https://doi.org/10.1080/09205063.2014.927300.
(22) Lee, I.; Kobayashi, K.; Sun, H. y.; Takatani, S.; Zhong, L. g. Biomembrane Mimetic Polymer Poly (2-Methacryloyloxyethyl Phosphorylcholine-Co-n-Butyl Methacrylate) at the Interface of Polyurethane Surfaces. *Journal of Biomedical Materials Research Part A* **2007**, *82A* (2), 316–322. https://doi.org/10.1002/jbm.a.30951.
(23) Hunger, J.; Ottosson, N.; Mazur, K.; Bonn, M.; Bakker, H. J. Water-Mediated Interactions between Trimethylamine-N-Oxide and Urea. *Phys. Chem. Chem. Phys.* **2014**, *17* (1), 298–306. https://doi.org/10.1039/C4CP02709D.
(24) Zhang, C.; Zhou, J.; Ye, X.; Li, Z.; Wang, Y. Zwitterionization of Tertiary Amines in Nanoporous Block Copolymers: Toward Fouling-Resistant Ultrafiltration Membranes. *Macromolecules* **2021**, *54* (9), 4236–4245. https://doi.org/10.1021/acs.macromol.1c00307.
(25) Huang, H.; Zhang, C.; Crisci, R.; Lu, T.; Hung, H.-C.; Sajib, M. S. J.; Sarker, P.; Ma, J.; Wei, T.; Jiang, S.; Chen, Z. Strong Surface Hydration and Salt Resistant Mechanism of a New Nonfouling Zwitterionic Polymer Based on Protein Stabilizer TMAO. *J. Am. Chem. Soc.* **2021**, *143* (40), 16786–16795. https://doi.org/10.1021/jacs.1c08280.
(26) Wang, J.; Paszti, Z.; Even, M. A.; Chen, Z. Measuring Polymer Surface Ordering Differences in Air and Water by Sum Frequency Generation Vibrational Spectroscopy. *J. Am. Chem. Soc.* **2002**, *124* (24), 7016–7023. https://doi.org/10.1021/ja012387r.
(27) Wang, H.-F.; Gan, W.; Lu, R.; Rao, Y.; Wu, B.-H. Quantitative Spectral and Orientational Analysis in Surface Sum Frequency Generation Vibrational Spectroscopy (SFG-VS). *International Reviews in Physical Chemistry* **2005**, *24* (2), 191–256. https://doi.org/10.1080/01442350500225894.
(28) Hankett, J. M.; Liu, Y.; Zhang, X.; Zhang, C.; Chen, Z. Molecular Level Studies of Polymer Behaviors at the Water Interface Using Sum Frequency Generation Vibrational Spectroscopy. *Journal of Polymer Science Part B: Polymer Physics* **2013**, *51* (5), 311–328. https://doi.org/10.1002/polb.23221.
(29) Lu, X.; Zhang, C.; Ulrich, N.; Xiao, M.; Ma, Y.-H.; Chen, Z. Studying Polymer Surfaces and Interfaces with Sum Frequency Generation Vibrational Spectroscopy. *Anal. Chem.* **2017**, *89* (1), 466–489. https://doi.org/10.1021/acs.analchem.6b04320.
(30) Wang, H.-F.; Velarde, L.; Gan, W.; Fu, L. Quantitative Sum-Frequency Generation Vibrational Spectroscopy of Molecular Surfaces and Interfaces: Lineshape, Polarization, and Orientation. *Annu Rev Phys Chem* **2015**, *66*, 189–216. https://doi.org/10.1146/annurev-physchem-040214-121322.

(31) Lu, R.; Gan, W.; Wu, B.; Zhang, Z.; Guo, Y.; Wang, H. C−H Stretching Vibrations of Methyl, Methylene and Methine Groups at the Vapor/Alcohol (n = 1−8) Interfaces. *J. Phys. Chem. B* **2005**, *109* (29), 14118–14129. https://doi.org/10.1021/jp051565q.
(32) Ohto, T.; Backus, E. H. G.; Mizukami, W.; Hunger, J.; Bonn, M.; Nagata, Y. Unveiling the Amphiphilic Nature of TMAO by Vibrational Sum Frequency Generation Spectroscopy. *J. Phys. Chem. C* **2016**, *120* (31), 17435–17443. https://doi.org/10.1021/acs.jpcc.6b04852.
(33) Tomar, D.; Rana, B.; Jena, K. C. The Structure of Water–DMF Binary Mixtures Probed by Linear and Nonlinear Vibrational Spectroscopy. *The Journal of Chemical Physics* **2020**, *152* (11), 114707. https://doi.org/10.1063/1.5141757.
(34) Ye, S.; Liu, G.; Li, H.; Chen, F.; Wang, X. Effect of Dehydration on the Interfacial Water Structure at a Charged Polymer Surface: Negligible χ(3) Contribution to Sum Frequency Generation Signal. *Langmuir* **2012**, *28* (2), 1374–1380. https://doi.org/10.1021/la203690p.
(35) Liu, G.; Wu, D.; Ma, C.; Zhang, G.; Wang, H.; Yang, S. Insight into the Origin of the Thermosensitivity of Poly[2-(Dimethylamino)Ethyl Methacrylate]. *ChemPhysChem* **2007**, *8* (15), 2254–2259. https://doi.org/10.1002/cphc.200700464.
(36) Ohno, P. E.; Wang, H.; Geiger, F. M. Second-Order Spectral Lineshapes from Charged Interfaces. *Nat Commun* **2017**, *8* (1), 1032. https://doi.org/10.1038/s41467-017-01088-0.
(37) Premadasa, U. I.; Bocharova, V.; Lin, L.; Genix, A.-C.; Heller, W. T.; Sacci, R. L.; Ma, Y.-Z.; Thiele, N. A.; Doughty, B. Tracking Molecular Transport Across Oil/Aqueous Interfaces: Insight into “Antagonistic” Binding in Solvent Extraction. *J. Phys. Chem. B* **2023**, *127* (21), 4886–4895. https://doi.org/10.1021/acs.jpcb.3c00386.
(38) Bui, T. T.; Colón, L. A.; Velarde, L. Intermolecular Interactions at the Silica–Liquid Interface Modulate the Fermi Resonance Coupling in Surface Methanol. *J. Phys. Chem. Lett.* **2021**, *12* (24), 5695–5702. https://doi.org/10.1021/acs.jpclett.1c01015.
(39) Lin, L.; Liu, Z.; Premadasa, U. I.; Li, T.; Ma, Y.-Z.; Sacci, R. L.; Katsaras, J.; Hong, K.; Collier, C. P.; Carrillo, J.-M. Y.; Doughty, B. The Unexpected Role of Cations in the Self-Assembly of Positively Charged Amphiphiles at Liquid/Liquid Interfaces. *J. Phys. Chem. Lett.* **2022**, *13* (46), 10889–10896. https://doi.org/10.1021/acs.jpclett.2c02921.
(40) Ostroverkhov, V.; Waychunas, G. A.; Shen, Y. R. New Information on Water Interfacial Structure Revealed by Phase-Sensitive Surface Spectroscopy. *Phys. Rev. Lett.* **2005**, *94* (4), 046102. https://doi.org/10.1103/PhysRevLett.94.046102.
(41) Ji, N.; Ostroverkhov, V.; Chen, C.-Y.; Shen, Y.-R. Phase-Sensitive Sum-Frequency Vibrational Spectroscopy and Its Application to Studies of Interfacial Alkyl Chains. *J. Am. Chem. Soc.* **2007**, *129* (33), 10056–10057. https://doi.org/10.1021/ja071989t.
(42) Kim, S.; Yang, Z.; Jakowski, J.; Ganesh, P.; Retterer, S. T.; Carrillo, J.-M. Y. All-Atom Modeling and Simulation of Biopolymer Interface: Dual Role of Antifouling Polymer Brushes. *Langmuir* **2025**, *41* (37), 25816–25826. https://doi.org/10.1021/acs.langmuir.5c03882.
(43) Flemming, P.; Janke, A.; Simon, F.; Fery, A.; Münch, A. S.; Uhlmann, P. Multiresponsive Transitions of PDMAEMA Brushes for Tunable Surface Patterning. *Langmuir* **2020**, *36* (50), 15283–15295. https://doi.org/10.1021/acs.langmuir.0c02711.
(44) Rehl, B.; Gibbs, J. M. Role of Ions on the Surface-Bound Water Structure at the Silica/Water Interface: Identifying the Spectral Signature of Stability. *J. Phys. Chem. Lett.* **2021**, *12* (11), 2854–2864. https://doi.org/10.1021/acs.jpclett.0c03565.
(45) Larini, L.; Shea, J.-E. Double Resolution Model for Studying TMAO/Water Effective Interactions. *J. Phys. Chem. B* **2013**, *117* (42), 13268–13277. https://doi.org/10.1021/jp403635g.
(46) Hunger, J.; Tielrooij, K.-J.; Buchner, R.; Bonn, M.; Bakker, H. J. Complex Formation in Aqueous Trimethylamine-N-Oxide (TMAO) Solutions. *J. Phys. Chem. B* **2012**, *116* (16), 4783–4795. https://doi.org/10.1021/jp212542q.

(47) Sarker, P.; Chen, G. T.; Sajib, M. S. J.; Jones, N. W.; Wei, T. Hydration and Antibiofouling of TMAO-Derived Zwitterionic Polymers Surfaces Studied with Atomistic Molecular Dynamics Simulations. *Colloids and Surfaces A: Physicochemical and Engineering Aspects* **2022**, *653*, 129943. https://doi.org/10.1016/j.colsurfa.2022.129943.
(48) Aissaoui, N.; Bergaoui, L.; Landoulsi, J.; Lambert, J.-F.; Boujday, S. Silane Layers on Silicon Surfaces: Mechanism of Interaction, Stability, and Influence on Protein Adsorption. *Langmuir* **2012**, *28* (1), 656–665. https://doi.org/10.1021/la2036778.
(49) Zoppe, J. O.; Ataman, N. C.; Mocny, P.; Wang, J.; Moraes, J.; Klok, H.-A. Surface-Initiated Controlled Radical Polymerization: State-of-the-Art, Opportunities, and Challenges in Surface and Interface Engineering with Polymer Brushes. *Chem. Rev.* **2017**, *117* (3), 1105–1318. https://doi.org/10.1021/acs.chemrev.6b00314.
(50) Feng, W.; Brash, J. L.; Zhu, S. Non-Biofouling Materials Prepared by Atom Transfer Radical Polymerization Grafting of 2-Methacryloloxyethyl Phosphorylcholine: Separate Effects of Graft Density and Chain Length on Protein Repulsion. *Biomaterials* **2006**, *27* (6), 847–855. https://doi.org/10.1016/j.biomaterials.2005.07.006.
(51) Premadasa, U. I.; Dong, D.; Stamberga, D.; Custelcean, R.; Roy, S.; Ma, Y.-Z.; Bocharova, V.; Bryantsev, V. S.; Doughty, B. Chemical Feedback in the Self-Assembly and Function of Air–Liquid Interfaces: Insight into the Bottlenecks of CO2 Direct Air Capture. *ACS Appl. Mater. Interfaces* **2023**, *15* (15), 19634–19645. https://doi.org/10.1021/acsami.3c00719.
(52) Chowdhury, A. U.; Liu, F.; Watson, B. R.; Ashkar, R.; Katsaras, J.; Collier, C. P.; Lutterman, D. A.; Ma, Y.-Z.; Calhoun, T. R.; Doughty, B. Flexible Approach to Vibrational Sum-Frequency Generation Using Shaped near-Infrared Light. *Opt. Lett., OL* **2018**, *43* (9), 2038–2041. https://doi.org/10.1364/OL.43.002038.
(53) Chowdhury, A. U.; Watson, B. R.; Ma, Y.-Z.; Sacci, R. L.; Lutterman, D. A.; Calhoun, T. R.; Doughty, B. A New Approach to Vibrational Sum Frequency Generation Spectroscopy Using near Infrared Pulse Shaping. *Review of Scientific Instruments* **2019**, *90* (3), 033106. https://doi.org/10.1063/1.5084971.
(54) Lu, X.; Clarke, M. L.; Li, D.; Wang, X.; Xue, G.; Chen, Z. A Sum Frequency Generation Vibrational Study of the Interference Effect in Poly(n-Butyl Methacrylate) Thin Films Sandwiched between Silica and Water. *J. Phys. Chem. C* **2011**, *115* (28), 13759–13767. https://doi.org/10.1021/jp202416z.
(55) Dramstad, T. A.; Wu, Z.; Massari, A. M. Sum Frequency Generation as a Proxy for Ellipsometry: Not Just a Phase. *The Journal of Chemical Physics* **2022**, *156* (11), 110901. https://doi.org/10.1063/5.0076252.
(56) Cotton, D. E.; Roberts, S. T. Sensitivity of Sum Frequency Generation Experimental Conditions to Thin Film Interference Effects. *The Journal of Chemical Physics* **2021**, *154* (11), 114704. https://doi.org/10.1063/5.0039897.
(57) Liljeblad, J. F. D.; Tyrode, E. Vibrational Sum Frequency Spectroscopy Studies at Solid/Liquid Interfaces: Influence of the Experimental Geometry in the Spectral Shape and Enhancement. *J. Phys. Chem. C* **2012**, *116* (43), 22893–22903. https://doi.org/10.1021/jp306838a.
(58) Khan, Md. R.; Premadasa, U. I.; Cimatu, K. L. A. Role of the Cationic Headgroup to Conformational Changes Undergone by Shorter Alkyl Chain Surfactant and Water Molecules at the Air-Liquid Interface. *Journal of Colloid and Interface Science* **2020**, *568*, 221–233. https://doi.org/10.1016/j.jcis.2020.02.056.
(59) Phillips, J. C.; Braun, R.; Wang, W.; Gumbart, J.; Tajkhorshid, E.; Villa, E.; Chipot, C.; Skeel, R. D.; Kalé, L.; Schulten, K. Scalable Molecular Dynamics with NAMD. *Journal of Computational Chemistry* **2005**, *26* (16), 1781–1802. https://doi.org/10.1002/jcc.20289.
(60) Vanommeslaeghe, K.; MacKerell, A. D. Jr. Automation of the CHARMM General Force Field (CGenFF) I: Bond Perception and Atom Typing. *J. Chem. Inf. Model.* **2012**, *52* (12), 3144–3154. https://doi.org/10.1021/ci300363c.

(61) Vanommeslaeghe, K.; Hatcher, E.; Acharya, C.; Kundu, S.; Zhong, S.; Shim, J.; Darian, E.; Guvench, O.; Lopes, P.; Vorobyov, I.; Mackerell Jr., A. D. CHARMM General Force Field: A Force Field for Drug-like Molecules Compatible with the CHARMM All-Atom Additive Biological Force Fields. *Journal of Computational Chemistry* **2010**, *31* (4), 671–690. https://doi.org/10.1002/jcc.21367.
(62) Vanommeslaeghe, K.; Raman, E. P.; MacKerell, A. D. Jr. Automation of the CHARMM General Force Field (CGenFF) II: Assignment of Bonded Parameters and Partial Atomic Charges. *J. Chem. Inf. Model.* **2012**, *52* (12), 3155–3168. https://doi.org/10.1021/ci3003649.
(63) Heinz, H.; Lin, T.-J.; Kishore Mishra, R.; Emami, F. S. Thermodynamically Consistent Force Fields for the Assembly of Inorganic, Organic, and Biological Nanostructures: The INTERFACE Force Field. *Langmuir* **2013**, *29* (6), 1754–1765. https://doi.org/10.1021/la3038846.
(64) Price, D. J.; Brooks, C. L., III. A Modified TIP3P Water Potential for Simulation with Ewald Summation. *The Journal of Chemical Physics* **2004**, *121* (20), 10096–10103. https://doi.org/10.1063/1.1808117.
(65) Essmann, U.; Perera, L.; Berkowitz, M. L.; Darden, T.; Lee, H.; Pedersen, L. G. A Smooth Particle Mesh Ewald Method. *The Journal of Chemical Physics* **1995**, *103* (19), 8577–8593. https://doi.org/10.1063/1.470117.
(66) Ryckaert, J.-P.; Ciccotti, G.; Berendsen, H. J. C. Numerical Integration of the Cartesian Equations of Motion of a System with Constraints: Molecular Dynamics of *n*-Alkanes. *Journal of Computational Physics* **1977**, *23* (3), 327–341. https://doi.org/10.1016/0021-9991(77)90098-5.
(67) Choi, Y. K.; Kern, N. R.; Kim, S.; Kanhaiya, K.; Afshar, Y.; Jeon, S. H.; Jo, S.; Brooks, B. R.; Lee, J.; Tadmor, E. B.; Heinz, H.; Im, W. CHARMM-GUI Nanomaterial Modeler for Modeling and Simulation of Nanomaterial Systems. *J. Chem. Theory Comput.* **2022**, *18* (1), 479–493. https://doi.org/10.1021/acs.jctc.1c00996.
(68) Feller, S. E.; Zhang, Y.; Pastor, R. W.; Brooks, B. R. Constant Pressure Molecular Dynamics Simulation: The Langevin Piston Method. *The Journal of Chemical Physics* **1995**, *103* (11), 4613–4621. https://doi.org/10.1063/1.470648.

For Table of Contents Only